COMPDYN 2013
4th ECCOMAS Thematic Conference on
Computational Methods in Structural Dynamics and Earthquake Engineering
M. Papadrakakis, V. Papadopoulos, V. Plevris (eds.)
Kos Island, Greece, 12–14 June 2013

A NUMERICAL STUDY OF SUBGRADE STIFFENING AS A MITIGATION MEASURE FOR RAILWAY INDUCED VIBRATIONS THROUGH 2.5D AND 3D FE–BE MODELS

Pieter Coulier, Stijn François, Geert Degrande, and Geert Lombaert

KU Leuven, Department of Civil Engineering
Kasteelpark Arenberg 40, 3001 Leuven, Belgium
e-mail: {pieter.coulier,stijn.francois,geert.degrande,geert.lombaert}@bwk.kuleuven.be

Keywords: Railway induced vibrations, dynamic soil–structure interaction, elastodynamic wave propgation, finite element–boundary element coupling.

Abstract. *This paper studies the efficiency of subgrade stiffening next to the track as a mitigation measure for railway induced vibrations. A computationally efficient two-and-a-half-dimensional (2.5D) methodology is first employed, assuming invariance of the geometry in the longitudinal direction. An analysis in the frequency–wavenumber domain reveals that an infinitely long block of stiffened soil next to the track can act as a wave impeding barrier. It is demonstrated that the wave impeding effect depends on the relation between the Rayleigh wavelength in the soil and the free bending wavelength in the block of stiffened soil, as the transmission of plane waves in the soil with a longitudinal wavelength smaller than the bending wavelength is hindered. This leads to a critical frequency from which this mitigation measure starts to be effective, depending on the stiffness contrast between the soil and the block of stiffened soil. The existence of a critical angle delimiting an area where vibration levels are reduced in case of harmonic excitation on the rail is also demonstrated. Fully three–dimensional (3D) calculations are finally performed to assess the vibration reduction efficiency if subgrade stiffening is only implemented along a finite length, indicating that the length of the block should be approximately two times the free bending wavelength of an infinitely long beam in order to ensure that a finite block can act as a wave impeding barrier.*

1 INTRODUCTION

Railway induced vibrations are an important source of annoyance in the built environment. Vibrations in buildings (1–80 Hz) can disturb sensitive equipment and cause discomfort to inhabitants, while re–radiated noise (16–250 Hz) may be perceived when bending resonances of floors and walls are excited.

During the last decades, a lot of research has been performed to obtain efficient and cost-effective vibration countermeasures [1, 2]. Three categories of vibration reduction methods can generally be distinguished. The most effective way is to tackle the problem at the source as this affects all nearby structures. These methods include the use of ballast mats [3], soft railpads [4], under–sleeper pads [5] and floating slab tracks [6] and are frequently used for new railway infrastructure. Interventions on the propagation path between source and receiver, such as an open trench in the soil [7], form a second category of methods to reduce the vibration levels. Their main advantage is that no modifications of the track are required, but their implementation may, however, be infeasible due to practical limitations. The third category of vibration reduction methods consists of measures taken at the receiver side, such as base isolation [8]; these are only effective for the structure where the mitigation measure is applied to.

Renewed attention has recently been paid to vibration reduction technologies on the transmission path, but installed close to the track as part of the railway infrastructure [9]. These measures include vibration isolation screens [10, 11], buried wall barriers [12], subgrade stiffening [13, 14], wave impeding blocks [15, 16] and wave reflectors [17]. Subgrade stiffening is often applied under railway tracks on soft soils with the aim of reducing settlements or track displacements [18]. Common techniques to obtain the desired stiffening include deep vibro compaction, deep soil mixing, gravel or cement columns, hydraulic fracture injection with stable cement-bentonite mixtures, and vacuum consolidation [19]. Subgrade stiffening is also known to lead to reduced ground-borne vibration levels due to the increase of the effective stiffness of the soil beneath the railway track. Vibrations are therefore expected to be reduced in the lower frequency range for all vehicle speeds and at all distances from the track. Subgrade stiffening seems to be a good solution for sites with an originally soft soil [13].

Although subgrade stiffening under the track is expected to be the most efficient way to reduce vibration levels, its practical implementation often requires interruption of train traffic and might cause uplifting of the track. This paper therefore focuses on subgrade stiffening next to the track, where a block of stiffened soil next to the track acts as a wave impeding vibration barrier. The effectiveness of the proposed mitigation measure is analyzed in section 2 assuming invariance of the geometry in the longitudinal direction, which allows for the application of a computationally efficient two-and-a-half-dimensional (2.5D) approach. The reduction of vibration levels is studied in case of harmonic excitation on the rail, as well as during the passage of a train, using a coupled finite element – boundary element (FE–BE) methodology. The construction of a jet grouting wall is in practice limited to finite dimensions, however, and the assumption of longitudinal invariance is therefore not fulfilled. A fast BE method based on hierarchical matrices [20] is employed in section 3 to solve the fully three–dimensional (3D) dynamic soil–structure interaction problem, allowing for the assessment of the vibration reduction efficiency if subgrade stiffening is only implemented along a finite length.

2 TWO–AND–A–HALF–DIMENSIONAL ANALYSIS

2.1 Dynamic properties of the track, the soil and the stiffened soil

Within the framework of the EU FP7 project RIVAS (Railway Induced Vibration Abatement Solutions) [9], a field test is planned in Spain to demonstrate the vibration reduction efficiency of subgrade stiffening next to the track. A conventional railway line on the Spanish network of ADIF between Barcelona and Gerona is therefore considered throughout this section; the track cross section is shown in figure 1. Although the soil properties at the site under consideration in reality vary with depth, the soil is assumed to be homogeneous in this paper in order to facilitate physical interpretation of the results. A halfspace with a shear wave velocity $C_\mathrm{s} = 200\,\mathrm{m/s}$, a dilatational wave velocity $C_\mathrm{p} = 400\,\mathrm{m/s}$, a density $\rho = 2000\,\mathrm{kg/m^3}$ and a material damping ratio $\beta_\mathrm{s} = \beta_\mathrm{p} = 0.025$ in both deviatoric and volumetric deformation is considered. The phase velocity C_R of the Rayleigh waves is equal to $186\,\mathrm{m/s}$ [21].

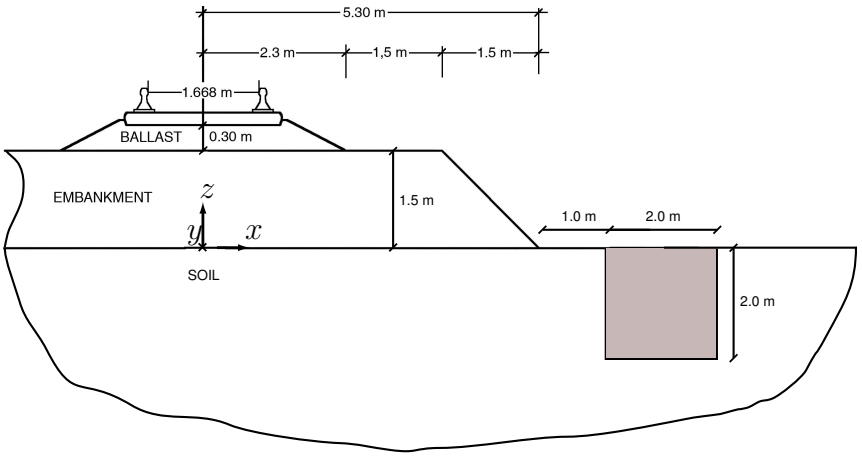

Figure 1: Track cross section.

The track consists of UIC 54 rails supported by rail pads on concrete sleepers, which are founded on a ballast layer and the embankment. The rails are modelled as Euler-Bernoulli beams with a bending stiffness $E_\mathrm{r}I_\mathrm{r} = 4.83 \times 10^6\ \mathrm{Nm^2}$ and a mass per unit length $\rho_\mathrm{r}A_\mathrm{r} = 54.4\,\mathrm{kg/m}$ for each rail. A wide track gauge of $1.668\,\mathrm{m}$ is used on this conventional Spanish track. The rail pads have a stiffness $k_\mathrm{rp} = 153.4 \times 10^6\,\mathrm{N/m}$ and a damping coefficient $c_\mathrm{rp} = 13.5 \times 10^3\,\mathrm{Ns/m}$. The following sleeper characteristics are considered: a length $l_\mathrm{sl} = 2.60\,\mathrm{m}$, a width $b_\mathrm{sl} = 0.250\,\mathrm{m}$, a height $h_\mathrm{sl} = 0.230\,\mathrm{m}$ (under the rail), a centre-to-centre distance $d_\mathrm{sl} = 0.60\,\mathrm{m}$ and a mass $m_\mathrm{sl} = 315\,\mathrm{kg}$.

A ballast layer with a thickness $t = 0.30$ m (under the sleepers) is also included in the track model. The ballast has a shear wave velocity $C_\mathrm{s} = 340\,\mathrm{m/s}$, a dilatational wave velocity $C_\mathrm{p} = 635\,\mathrm{m/s}$, a density $\rho = 1700\,\mathrm{kg/m^3}$ and a material damping ratio $\beta_\mathrm{s} = \beta_\mathrm{p} = 0.020$ in both deviatoric and volumetric deformation. The embankment has a thickness $t = 1.50\,\mathrm{m}$, a shear wave velocity $C_\mathrm{s} = 140\,\mathrm{m/s}$, a dilatational wave velocity $C_\mathrm{p} = 290\,\mathrm{m/s}$ and a density $\rho = 1700\ \mathrm{kg/m^3}$. The same material damping ratios as for the ballast are used. The remaining geometric dimensions of the ballast and embankment are indicated on figure 1.

The reference case outlined above is compared to the case where a block of soil with a width and depth of $2\,\mathrm{m}$ located at $1\,\mathrm{m}$ from the tail of the embankment is stiffened (figure 1). The block of stiffened soil has a shear wave velocity $C_\mathrm{s} = 550\,\mathrm{m/s}$, a dilatational wave velocity $C_\mathrm{p} = 950\,\mathrm{m/s}$, a density $\rho = 2000\,\mathrm{kg/m^3}$ and a material damping ratio $\beta_\mathrm{s} = \beta_\mathrm{p} = 0.050$ in both deviatoric and volumetric deformation.

2.2 The numerical model

Several subproblems have to be addressed in order to investigate the vibration reduction efficiency of subgrade stiffening next to the track, such as the train–track interaction problem which allows for the determination of the dynamic axle loads, the track–soil interaction problem for the calculation of the transfer functions, and the computation of the response to moving loads [22, 23].

The response in the free field at distances sufficiently far from the track is dominated by dynamic axle loads if the train speed is small compared to the Rayleigh wave velocity C_{R}. Although several mechanisms contribute to the generation of these dynamic axle loads, often only those originating from the track unevenness are taken into account [22]. This kind of dynamic excitation can be calculated based on a compliance formulation in a moving frame of reference, which requires the vehicle and track compliance. The interaction forces are subsequently combined with the transfer functions between the track and the free field, which are determined from the track–soil interaction problem.

The track–soil interaction problem is solved by means of a coupled FE–BE methodology formulated in the frequency domain [24]. The domains Ω_1 and Ω_2 are modelled by means of finite elements, while boundary elements on the soil–structure interfaces Σ_1 and Σ_2 are used to model the soil domain Ω_{s} (figure 2). Green's functions for a horizontally layered halfspace are used as fundamental solutions in the BE formulation [25, 26]. By assuming invariance of the geometry in the longitudinal direction, a computationally efficient two-and-a-half-dimensional (2.5D) approach can be applied. The longitudinal coordinate y is transformed to the wavenumber k_y by means of a forward Fourier transform, and all calculations can be performed in the frequency–wavenumber domain. Although the track has a periodic layout due to the discrete support of the sleepers, an equivalent continuous model is employed. An equivalent rail pad stiffness $\overline{k}_{\mathrm{rp}} = k_{\mathrm{rp}}/d_{\mathrm{sl}}$, damping coefficient $\overline{c}_{\mathrm{rp}} = c_{\mathrm{rp}}/d_{\mathrm{sl}}$ and a uniformly distributed sleeper mass $\overline{m}_{\mathrm{sl}} = m_{\mathrm{sl}}/d_{\mathrm{sl}}$ per unit length are calculated. The sleepers are assumed to be rigid in the plane of the track cross section and not to contribute to the longitudinal stiffness of the track. A detailed description of the governing equations of the equivalent continuous rails/rail pads/sleepers–system can be found in [22].

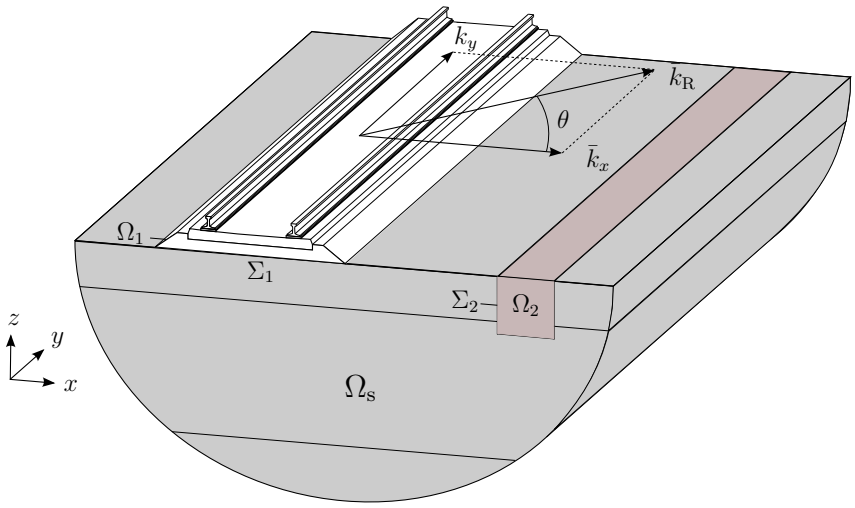

Figure 2: The 2.5D dynamic soil–structure interaction problem.

If N structures are considered, a weak variational formulation of the equilibrium of structure j ($j = 1, \ldots, N$) results in the following set of coupled FE–BE equations [24]:

$$\left[\tilde{\mathbf{K}}_j(k_y,\omega) - \omega^2 \mathbf{M}_j\right] \underline{\tilde{\mathbf{u}}}_j(k_y,\omega) + \sum_{k=1}^{N} \tilde{\mathbf{K}}^{\mathrm{s}}_{jk}(k_y,\omega)\underline{\tilde{\mathbf{u}}}_k(k_y,\omega) = \underline{\tilde{\mathbf{f}}}_j(k_y,\omega) \tag{1}$$

where a tilde above a variable denotes its representation in the frequency–wavenumber domain. $\underline{\tilde{\mathbf{u}}}_j(k_y,\omega)$ collects the nodal degrees of freedom of structure j, while $\tilde{\mathbf{K}}_j(k_y,\omega)$ and $\mathbf{M}_j$ are the finite element stiffness and mass matrix of this structure. $\tilde{\mathbf{K}}^{\mathrm{s}}_{jk}(k_y,\omega)$ is a dynamic soil stiffness matrix, representing the through–soil coupling of structures j and k for $j \neq k$, and is computed by means of the BE method. The force vector $\underline{\tilde{\mathbf{f}}}_j(k_y,\omega)$ results from the external forces on structure j [24]. In this paper, the number of structures N will be limited to $N = 1$ in the reference case (where only the track is considered) or $N = 2$ in the case a block of stiffened soil is introduced next to the track.

Figure 3 shows the finite element discretization. Eight–node quadrilateral finite elements are used to model the ballast, the embankment and the block of stiffened soil, which are coupled to a conforming BE mesh for the surrounding soil. The element dimensions are limited in order to ensure that at least 10 elements per minimal shear wavelength $\lambda_{\mathrm{s}} = 2\pi C_{\mathrm{s}}/\omega$ are used up to $100\,\mathrm{Hz}$ (determined by the shear wave velocity of the embankment), resulting in a maximum element size $l_e = 0.13\,\mathrm{m}$.

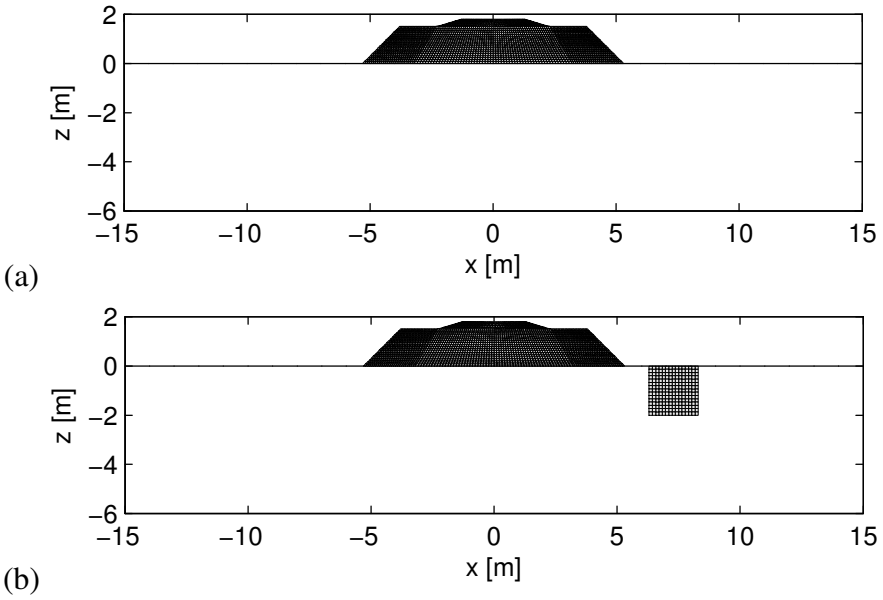

Figure 3: Finite element discretization (a) in the reference case and (b) in the case of stiffening next to the track.

Solving the set of coupled FE–BE equations (1) provides the structural response in the frequency–wavenumber domain. The wavenumber domain formulation of the integral representation theorem [24] subsequently allows for the calculation of the radiated wavefield in the soil. The response in the frequency–spatial domain can finally be found by means of an inverse Fourier transform.

The influence of subgrade stiffening on each of the aforementioned subproblems is investigated separately in the next subsections. The train–track and the track–soil interaction problems will be addressed in subsections 2.3 and 2.4, respectively, while the overall efficiency of

subgrade stiffening during the passage of a Renfe S599 train will finally be evaluated in subsection 2.6.

2.3 The track compliance in the frequency domain

The dynamic axle loads are computed by means of a compliance formulation in a moving frame of reference based on the vehicle compliance, the track compliance, and the track unevenness. It can be anticipated, however, that subgrade stiffening next to the track will only have a minor impact on the track compliance, so that the dynamic axle loads will not be affected. In order to verify this, the track compliance is computed by applying a unit harmonic vertical point load to the right rail at $y = 0\,\mathrm{m}$ in both cases. The response in the frequency–wavenumber domain is found from the solution of equation (1), and an inverse Fourier transform provides the response in the frequency–spatial domain.

Figure 4 shows that the rail receptance $\hat{u}_\mathrm{r}(y = 0\,\mathrm{m}, \omega)$ is not significantly modified by the presence of the block of stiffened soil next to the track, in the frequency range considered. The track compliance, and hence the dynamic axle loads, will remain unaffected, which implies that the efficiency of subgrade stiffening can be assessed by investigating the transfer functions only.

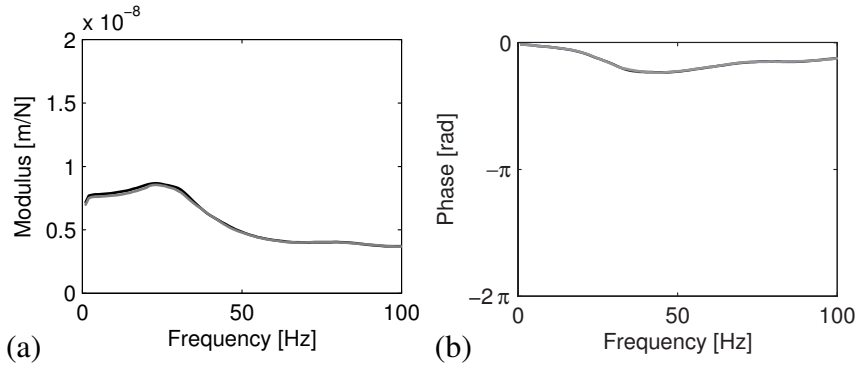

Figure 4: (a) Modulus and (b) phase of the rail receptance $\hat{u}_\mathrm{r}(y = 0\,\mathrm{m}, \omega)$ in the reference case (black line) and in the case of stiffening next to the track (grey line).

2.4 The free field impulse response in the frequency–wavenumber domain

As indicated in subsection 2.2, the radiated wavefield in the soil in the frequency–wavenumber domain can be obtained by application of the integral representation theorem [24]. The logarithm of the modulus of the vertical free field velocity $i\omega\tilde{u}_z\left(x = 64\,\mathrm{m}, \bar{k}_y, z = 0\,\mathrm{m}, \omega\right)$ is shown in figures 5a and 5b as a function of the dimensionless longitudinal wavenumber $\bar{k}_y$ and the frequency $\omega/2\pi$ in the reference case and in the case of stiffening next to the track, respectively. The dimensionless wavenumber $\bar{k}_y$ is defined as $\bar{k}_y = k_y C_\mathrm{s}/\omega = C_\mathrm{s}/C_y$, where C_s is the shear wave velocity of the halfspace and C_y is the phase velocity of the waves. Superimposed on both figures is the dispersion curve $\bar{k}_y = \bar{k}_\mathrm{R} = C_\mathrm{s}/C_\mathrm{R}$ of a Rayleigh wave propagating in the y-direction. This dispersion curve is a horizontal line $\bar{k}_\mathrm{R} = 1.073$ (as the halfspace has a Poisson's ratio $\nu = 1/3$) due to the non-dispersive character of the Rayleigh wave in a homogeneous halfspace.

The contribution of longitudinal wavenumbers $\bar{k}_y$ larger than $\bar{k}_\mathrm{R}$ to the free field response is very limited, as can be seen in figures 5a and 5b. This is due to the fact that the lateral

wavenumber $\bar{k}_x = -i\sqrt{\bar{k}_y^2 - \bar{k}_\mathrm{R}^2}$ is imaginary for $\bar{k}_y > \bar{k}_\mathrm{R}$, and the wave in the x-direction hence becomes evanescent.

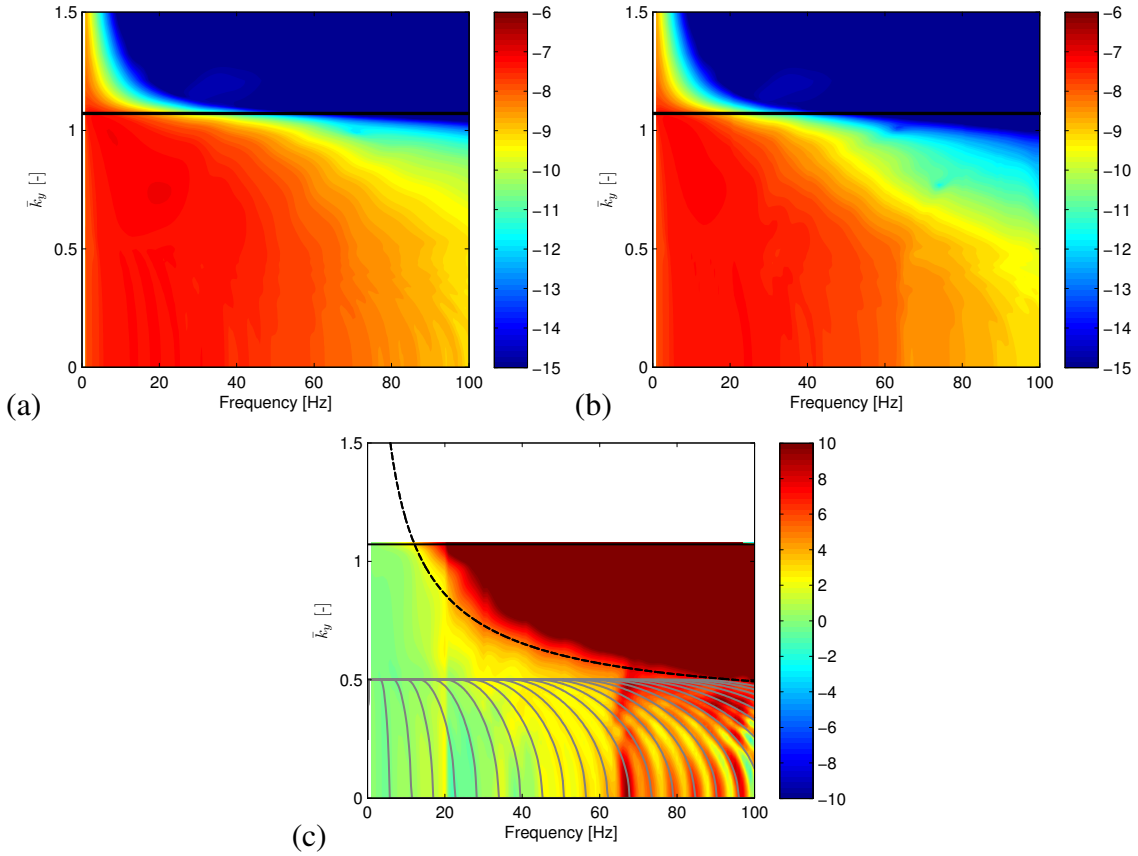

Figure 5: Logarithm of the modulus of the vertical free field velocity $i\omega\tilde{u}_z\left(x = 64\,\mathrm{m}, \bar{k}_y, z = 0\,\mathrm{m}, \omega\right)$ (a) in the reference case and (b) in the case of subgrade stiffening next to the track. The corresponding insertion loss $\widetilde{\mathrm{IL}}_z\left(x = 64\,\mathrm{m}, \bar{k}_y, z = 0\,\mathrm{m}, \omega\right)$ is shown in (c). Superimposed are the dispersion curve of a Rayleigh wave in the y-direction (solid black line), the free bending wave dispersion curve in an infinitely long beam (dashed black line) and the relation between $\bar{k}_y$ and ω given by equation (9) (solid grey lines).

The efficiency of a mitigation measure can be quantified in the frequency–wavenumber domain through the vertical insertion loss $\widetilde{\mathrm{IL}}_z(x, \bar{k}_y, z, \omega)$:

$$\widetilde{\mathrm{IL}}_z(x, \bar{k}_y, z, \omega) = 20\log_{10}\frac{|\tilde{u}_z^{\mathrm{ref}}(x, \bar{k}_y, z, \omega)|}{|\tilde{u}_z(x, \bar{k}_y, z, \omega)|} \qquad [\mathrm{dB}] \tag{2}$$

Positive values of the insertion loss indicate a reduction of the vertical free field vibrations. Figure 5c shows the insertion loss $\widetilde{\mathrm{IL}}_z\left(x = 64\,\mathrm{m}, \bar{k}_y, z = 0\,\mathrm{m}, \omega\right)$. The insertion loss is only shown in a range $0 \leq \bar{k}_y \leq \bar{k}_\mathrm{R}$, as propagating waves only exist in this range. A clearly delimited area in the $(\bar{k}_y, \omega)$–domain corresponding to a significant insertion loss can be distinguished in this figure.

Figure 5c can physically be explained by regarding the block of stiffened soil as an infinitely long beam. The partial differential equation describing the transverse displacement $u_z(y, t)$ of a Timoshenko beam can be transformed to the frequency–wavenumber domain and reads as

follows [27]:

$$\left(-\rho A\omega^2 + EIk_y^4 - \rho I\left(1+\frac{E}{\kappa\mu}\right)\omega^2 k_y^2 + \frac{\rho^2 I}{\kappa\mu}\omega^4\right)\tilde{u}_z(k_y,\omega) = \tilde{f}(k_y,\omega) \tag{3}$$

where E is the Young's modulus, μ the shear modulus, ρ the density, A the cross sectional area, I the moment of inertia for bending with respect to the horizontal axis and κ the shear coefficient of the beam. Figure 6 shows the normalized admittance $|\tilde{Y}(\bar{k}_y,\omega)/\tilde{Y}(\bar{k}_y=0,\omega)|$, where the admittance $\tilde{Y}(k_y,\omega)$ is defined as the ratio of the transverse velocity $i\omega\tilde{u}_z(k_y,\omega)$ and the external loading $\tilde{f}(k_y,\omega)$. The dimensionless wavenumber $\bar{k}_y$ is defined as above.

The dispersion relation follows from equation (3) and can be written as:

$$\left(-\frac{E}{\rho}k_y^2+\omega^2\right)\left(-\frac{\kappa\mu}{\rho}k_y^2+\omega^2\right) - \frac{\kappa\mu A}{\rho I}\omega^2 = 0 \tag{4}$$

The dispersion relation (4) comprises two branches of the dispersion curve, corresponding to a bending and shear mode, respectively [27]. Below a certain radial cut-on frequency equal to $\sqrt{\frac{\kappa\mu A}{\rho I}}$, there is a single branch which corresponds to real wavenumbers, and thus a propagating (bending) mode. The cut-on frequency equals $2\pi \times 138\,\mathrm{Hz}$ in the present case, which implies that only the bending mode is of importance in the frequency range considered.

Superimposed on figure 6 is the dispersion curve $\bar{k}_y = \bar{k}_\mathrm{b}$ of a free bending wave in the beam which satisfies the dispersion relation (4). This figure clearly illustrates that the amplitude of propagating bending waves in a beam becomes very small for wavenumbers $\bar{k}_y$ larger than $\bar{k}_\mathrm{b}$, which equivalently corresponds to wavelengths λ_y smaller than the free bending wavelength λ_b. The response is then dominated by the bending stiffness of the beam and the amplitude decreases proportionally to k_y^{-4} at a given radial frequency ω (cfr. equation (3)).

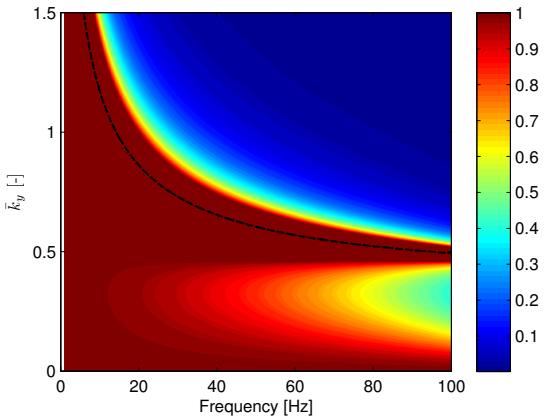

Figure 6: Normalized admittance $|\tilde{Y}(\bar{k}_y,\omega)/\tilde{Y}(\bar{k}_y=0,\omega)|$ of a beam with the dynamic properties of the block of stiffened soil next to the track. Superimposed is the free bending wave dispersion curve (dashed black line).

Figure 5c can now be interpreted based on the interaction of the Rayleigh wave in the soil and bending waves in the block of stiffened soil. At low frequencies, the wavenumber $\bar{k}_\mathrm{b}$ is larger than the wavenumber $\bar{k}_\mathrm{R}$, and the Rayleigh wave propagates through the block of stiffened soil. From a critical frequency on, the wavefield contains propagating plane waves ($\bar{k}_y \leq \bar{k}_\mathrm{R}$) with a wavenumber $\bar{k}_y$ larger than $\bar{k}_\mathrm{b}$ (i.e. with a wavelength λ_y smaller than λ_b). The transmission

of these plane waves is impeded by the block of stiffened soil as soon as $\bar{k}_y$ is slightly larger than $\bar{k}_\mathrm{b}$ (cfr. figure 6). This explains why the zone of significant insertion loss in figure 5c is clearly delimited by the free bending wave dispersion curve. The critical radial frequency ω_c from which the block of stiffened soil can act as a wave impeding barrier is determined by the intersection of the Rayleigh wave and the free bending wave dispersion curves:

$$\omega_\mathrm{c} = C_\mathrm{R}^2 \sqrt{\frac{\rho A}{EI}} \sqrt{\frac{E\mu\kappa}{\left(E - \rho C_\mathrm{R}^2\right)\left(\mu\kappa - \rho C_\mathrm{R}^2\right)}} \tag{5}$$

which equals $2\pi \times 12\,\mathrm{Hz}$ in the actual case. If the shear deformation and rotational inertia of the block of stiffened soil are neglected, equation (3) reduces to the Euler–Bernoulli beam equation, and the critical frequency can be approximated as:

$$\omega_\mathrm{c} \simeq C_\mathrm{R}^2 \sqrt{\frac{\rho A}{EI}} = \frac{C_\mathrm{R}^2}{h} \sqrt{\frac{12\rho}{E}} \tag{6}$$

where h is the depth of the block of stiffened soil, if bending with respect to the horizontal axis is considered. It is clear from the discussion above that the mitigation measure can only be effective for frequencies above ω_c. Equations (5) and (6) reveal that the critical frequency strongly depends on the stiffness contrast between the soil and the block of stiffened soil, indicating that this mitigation measure will be more effective at sites with a soft soil. These expressions furthermore illustrate that increasing the depth h of the stiffened block is beneficial, as this results in a reduction of the critical frequency. A minimal width is also required, however, in order to ensure that the block of stiffened soil behaves as a beam. Equation (6) is of great practical importance, as it provides a simple design guideline to assess the expected vibration reduction efficiency of soil stiffening next to the track, without the need of an extensive FE–BE calculation.

The physical mechanism outlined above closely resembles the phenomenon of coincidence in acoustics [28], where sound waves impinging on an infinite plate are freely transmitted if the wavelength of bending waves in the plate equals the trace wavelength of the acoustic waves in the air. In acoustics, the transmission loss below coincidence is predominantly related to the so-called mass law [28]. At the coincidence frequency, a prominent dip occurs in the transmission loss. At higher frequencies, the transmission loss increases significantly due to the increased bending stiffness. In the present case, a reduction of vibration levels is only seen above coincidence, attributed to the bending stiffness of the block of stiffened soil next to the track, while the inertia effect is negligible. An increase of the density with respect to the original soil is, however, also expected to be beneficial.

The propagating plane waves ($\bar{k}_y \leq \bar{k}_\mathrm{R}$) are characterized by a wave propagation direction $\theta = \sin^{-1}\left(\bar{k}_y / \bar{k}_\mathrm{R}\right)$ (figure 2). As a result, a reduction of vibration levels will only be obtained in an area delimited by a critical angle $\theta_\mathrm{c}(\omega) = \sin^{-1}\left(\bar{k}_\mathrm{b} / \bar{k}_\mathrm{R}\right)$, defined as:

$$\sin\theta_\mathrm{c}(\omega) = C_\mathrm{R} \sqrt{\rho \frac{E + \mu\kappa \pm \sqrt{\left(E - \mu\kappa\right)^2 + \frac{4E(\mu\kappa)^2 A}{\rho I \omega^2}}}{2E\mu\kappa}} \tag{7}$$

where the plus and minus signs correspond to the first and second branch of the beam dispersion curve, respectively. As indicated above, only the first branch is of interest in the frequency

range considered. At limiting high frequencies, the critical angle related to this branch can be approximated as:

$$\sin\theta_{\mathrm{c}} = C_{\mathrm{R}}\sqrt{\frac{\rho}{\mu\kappa}} \tag{8}$$

Figure 5c furthermore exhibits a regular pattern of regions where an increased insertion loss can be observed, for $0 < \bar{k}_y < s$, where $s = C_{\mathrm{s}}/C_{\mathrm{p}} = 0.5$ in the present case. This can be explained by the fact that the P-wave travels faster through the block of stiffened soil than in the halfspace, which introduces a phase shift between the wave fronts in the reference case and in the case where stiffening next to the track is included. The following expression gives the relation between wavenumbers $\bar{k}_y$ and radial frequencies ω which result in a phase shift equal to a multiple of 2π:

$$\left(\sqrt{\left(\frac{\omega}{C_{\mathrm{R}}}\right)^2 - \left(\frac{\bar{k}_y\omega}{C_{\mathrm{s}}}\right)^2} - \sqrt{\left(\frac{\omega}{C_{\mathrm{p}}}\right)^2 - \left(\frac{\bar{k}_y\omega}{C_{\mathrm{s}}}\right)^2}\right) x - \omega\frac{w}{\Delta C_{\mathrm{p}}} = 2\pi n \quad \text{for} \quad n = 0, 1, 2, \ldots \tag{9}$$

with $x = 64\,\mathrm{m}$ the location under consideration, $w = 2\,\mathrm{m}$ the width of the block of stiffened soil and $\Delta C_{\mathrm{p}} = 550\,\mathrm{m/s}$ the difference in dilatational wave velocities between the halfspace and the stiffened block. The square roots between brackets are the dimensionless lateral wavenumbers $\bar{k}_{x\mathrm{R}}$ for the Rayleigh wave and $\bar{k}_{x\mathrm{p}}$ for the P-wave, respectively, while the term $\omega w/\Delta C_{\mathrm{p}}$ denotes the phase shift. Lines corresponding to the relation given by equation (9) are superimposed on figure 5c. These lines coincide almost perfectly with the regions where an increased insertion loss is observed, especially at frequencies above $50\,\mathrm{Hz}$, as the wavelength in the soil then becomes comparable to the dimensions of the block of stiffened soil.

The physical mechanism that determines the effectiveness of subgrade stiffening next to the track has been interpreted in the frequency–wavenumber domain. In the following, it is shown how this mechanism becomes apparent in the frequency–spatial domain.

2.5 The free field impulse response in the frequency–spatial domain

The track and soil response in the frequency–spatial domain can be found by means of an inverse Fourier transform. Figures 7a and 7b show the real part of the vertical displacement $\hat{u}_z(\mathbf{x},\omega)$ at $5\,\mathrm{Hz}$ in the reference case and in the case of stiffening next to the track, respectively, due to a unit harmonic vertical point load applied to the right rail at $y = 0\,\mathrm{m}$. The Rayleigh wavelength $\lambda_{\mathrm{R}} = 2\pi C_{\mathrm{R}}/\omega$ in the soil is much larger than the width of the track, resulting in a wave field characterized by nearly cylindrical wave fronts. The corresponding insertion loss $\widehat{\mathrm{IL}}_z(\mathbf{x},\omega)$ is shown in figure 7c. As the considered frequency is smaller than the critical frequency $\omega_{\mathrm{c}}/2\pi$, the block of stiffened soil is unable to impede the propagation of the Rayleigh wave, and the insertion loss is zero almost everywhere in the soil domain.

Figure 8 shows the real part of the vertical displacement $\hat{u}_z(\mathbf{x},\omega)$ at a frequency of $30\,\mathrm{Hz}$, which is above the critical frequency $\omega_{\mathrm{c}}/2\pi$. The wave fronts at the surface of the soil are no longer cylindrical due to the dynamic interaction between the track and the halfspace. The critical angle at the considered frequency equals $\theta_{\mathrm{c}} = \sin^{-1}(0.73/1.073) = 43°$. This angle is indicated on figure 8c, which confirms that a significant reduction of vibration levels is obtained for $\theta > \theta_{\mathrm{c}}$. The insertion loss reaches values of $10\,\mathrm{dB}$ and more in this region. The reduction is not only obtained at the surface of the halfspace, but also at depth, although some localized areas

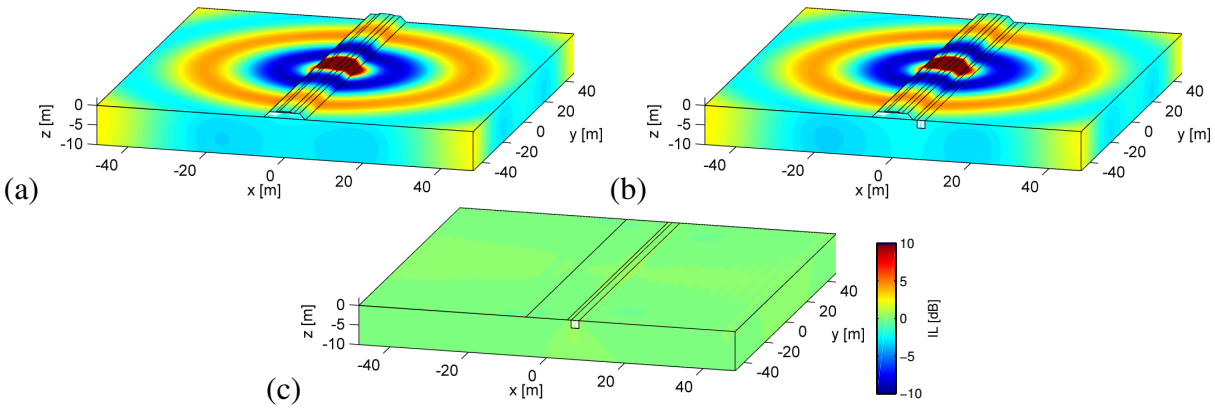

Figure 7: Real part of the vertical displacement $\hat{u}_z(\mathbf{x},\omega)$ due to harmonic excitation on the right rail at $5\,\mathrm{Hz}$ (a) in the reference case and (b) in the case of stiffening next to the track, and (c) the corresponding insertion loss $\widehat{\mathrm{IL}}_z(\mathbf{x},\omega)$.

can be identified with increased vibration levels with respect to the reference case. The angle $\sin^{-1}\left(s/\bar{k}_\mathrm{R}\right) = \sin^{-1}\left(0.50/1.073\right) = 28°$ is also indicated on figure 8c, which delimits the area where an interference pattern as considered in equation (9) is visible. Lines of constructive and destructive interference between direct and reflected Rayleigh waves can furthermore be observed at the opposite side of the track (i.e. where no soil stiffening is applied).

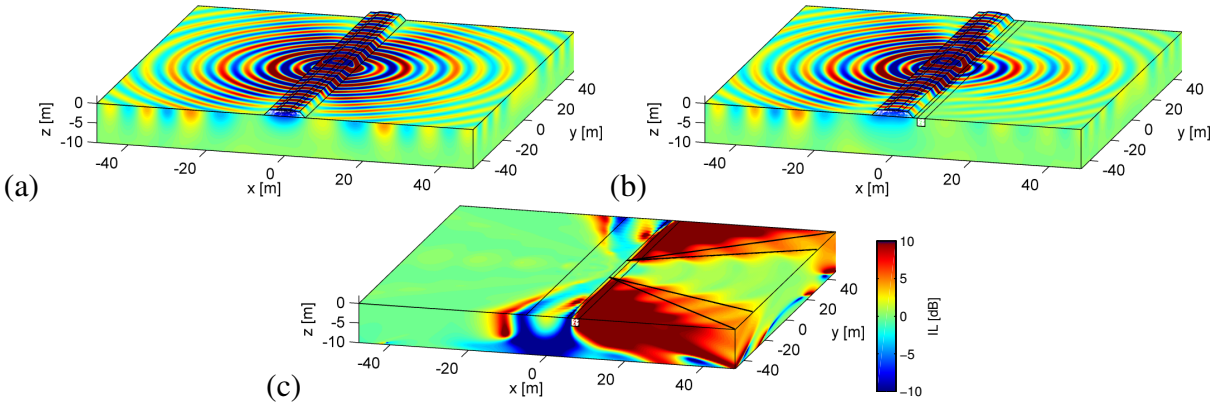

Figure 8: Real part of the vertical displacement $\hat{u}_z(\mathbf{x},\omega)$ due to harmonic excitation on the right rail at $30\,\mathrm{Hz}$ (a) in the reference case and (b) in the case of stiffening next to the track, and (c) the corresponding insertion loss $\widehat{\mathrm{IL}}_z(\mathbf{x},\omega)$.

Figure 9 shows the real part of the vertical displacement $\hat{u}_z(\mathbf{x},\omega)$ at a frequency of $60\,\mathrm{Hz}$. As in figure 8, the wave fronts are not cylindrical. The critical angle at this frequency is $\theta_\mathrm{c} = \sin^{-1}(0.57/1.073) = 32°$, and is clearly visible in figure 9c. The interference pattern in the area bounded by the angle $\sin^{-1}\left(s/\bar{k}_\mathrm{R}\right)$ is even more clear than in figure 8. Lines of constructive and destructive interference at the opposite side of the track can be observed as well.

It follows from the previous discussion that a reduction of vibration levels is only obtained above the critical frequency $\omega_\mathrm{c}/2\pi$, predominantly in the area delimited by the critical angle $\theta_\mathrm{c}(\omega)$. The reduction on a line perpendicular to the track at the position where the load is applied is less than in other points. This is confirmed in figure 10, which shows the free field mobility at a lateral distance of $24\,\mathrm{m}$ from the center of the track, at $y = 0\,\mathrm{m}$ and at $y = 24\,\mathrm{m}$. This implies

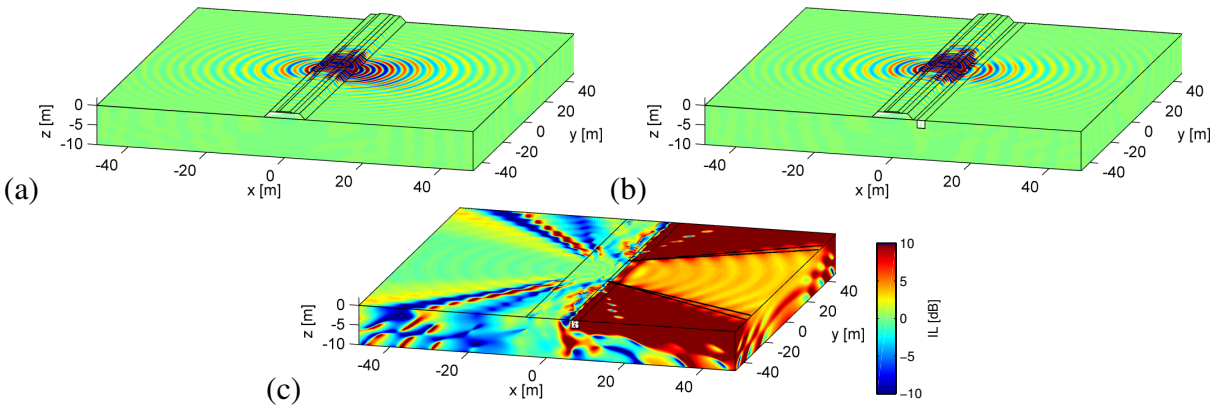

Figure 9: Real part of the vertical displacement $\hat{u}_z(\mathbf{x},\omega)$ due to harmonic excitation on the right rail at $60\,\mathrm{Hz}$ (a) in the reference case and (b) in the case of stiffening next to the track, and (c) the corresponding insertion loss $\widehat{\mathrm{IL}}_z(\mathbf{x},\omega)$.

that, if the passage of a train is considered, the contribution of the dynamic axle loads moving towards or away from a receiver will be mitigated more effectively than the contribution of the dynamic axle loads located close to the receiver. The passage of a train is discussed in more detail in the next subsection.

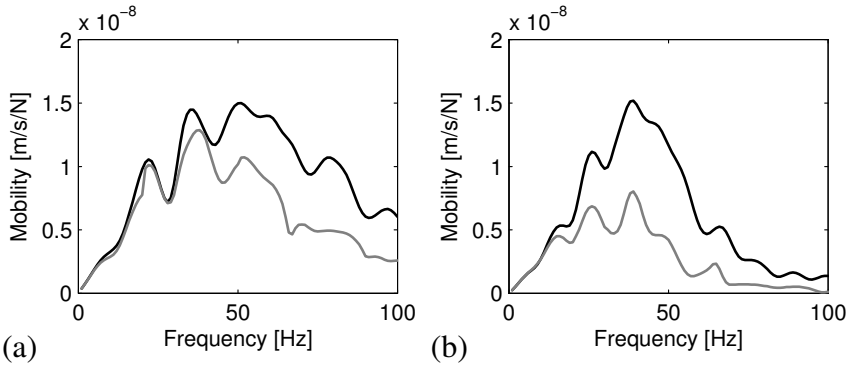

Figure 10: Free field mobility at $x = 24\,\mathrm{m}$ and (a) $y = 0\,\mathrm{m}$ and (b) $y = 24\,\mathrm{m}$ in the reference case (black line) and in the case of stiffening next to the track (grey line).

2.6 The free field response during the passage of a Renfe S599 train

Finally, the vibration reduction efficiency of the proposed mitigation measure during the passage of a Renfe S599 train at a speed of $160\,\mathrm{km/h}$ is investigated. This type of train consists of two motor coaches and a central carriage and has a total length of $75.98\,\mathrm{m}$. Each carriage is supported by two bogies and has four axles. The number of axles N_a, the carriage length L_t, the distance L_b between bogies, the axle distance L_a, and the unsprung axle mass M_u of the carriages are summarized in table 1. Only these unsprung masses are taken into account, as the carriage's primary and secondary suspension isolate the body and the bogie from the wheelset at frequencies above a few Hertz [29].

As indicated in subsection 2.2, only the dynamic axle loads originating from the track unevenness are taken into account. A track with an unevenness profile according to the FRA class 3 [30] is assumed. The free field velocity due to a train passage is characterized by an in-

	N_a $[-]$	L_t $[\mathrm{m}]$	L_b $[\mathrm{m}]$	L_a $[\mathrm{m}]$	M_u $[\mathrm{kg}]$
Two motor coaches	4	25.85	17.73	2.50	1940
One central carriage	4	24.28	18.00	2.50	1704

Table 1: Characteristics of the Renfe S599 train.

creasing vibration level when the train is approaching, a nearly stationary vibration level during the passage of the train and a decreasing vibration level when the train is moving away. It has been shown that the dominating stationary part of the free field velocity can be well approximated by a prediction in which the dynamic axle loads are applied at fixed positions [31]. This approach is employed throughout this section.

Figure 11 shows the one–third octave band RMS spectra of the vertical free field vibration velocity during the passage of a Renfe S599 train at a speed of $160\,\mathrm{km/h}$. In the reference case, the frequency content of the free field vibrations close to the track is mainly situated in a frequency range between $20\,\mathrm{Hz}$ and $100\,\mathrm{Hz}$, while at larger distances from the track, material damping in the soil results in a strong attenuation of the response at high frequencies. In the case of subgrade stiffening next to the track, a reduction of vibration levels is obtained above the critical frequency of $12\,\mathrm{Hz}$. Superimposed on figure 11 are ISO vibration criterion curves for the effect of vibrations on people in buildings [32], indicating that subgrade stiffening can be used as an effective mitigation measure in order to comply with vibration criteria. Subgrade stiffening has furthermore a negligible effect on the vibration levels at the opposite side of the track, as the interference patterns observable in case of harmonic excitation (cfr. figures 8c and 9c) cancel each other out during the passage of a train.

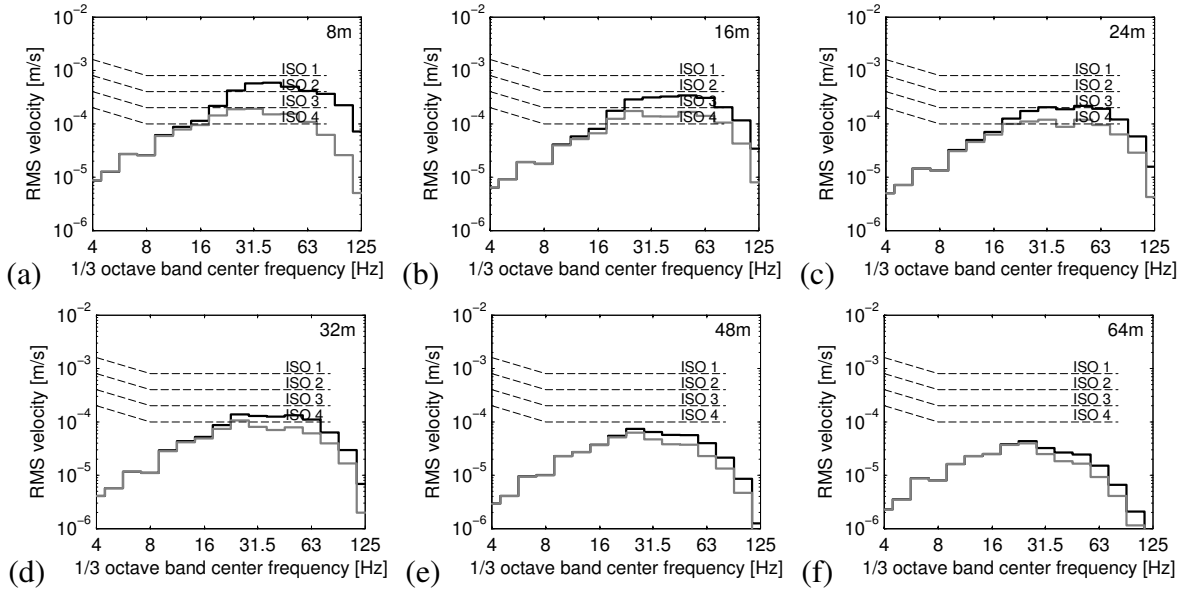

Figure 11: One–third octave band RMS spectra of the vertical free field vibrations in the reference case (black line) and in the case of stiffening next to the track (grey line) at a distance of (a) $8\,\mathrm{m}$, (b) $16\,\mathrm{m}$, (c) $24\,\mathrm{m}$, (d) $32\,\mathrm{m}$, (e) $48\,\mathrm{m}$ and (f) $64\,\mathrm{m}$ from the center of the track due to the passage of a Renfe S599 train at a speed of $160\,\mathrm{km/h}$.

The efficiency of the mitigation measure is investigated in more detail in figure 12, which shows the vertical insertion loss $\widehat{\mathrm{IL}}_z(\mathbf{x},\omega)$ for several locations at increasing distance from the

track. The insertion loss is defined in a similar way as in equation (2), but now for the one–third octave band RMS spectra of the vertical free field vibration velocity. This figure clearly confirms that a reduction can be obtained above the critical frequency $\omega_c/2\pi$. Generally speaking, the insertion loss is higher at locations closer to the track, while an increase of insertion loss with frequency can be observed at a particular location.

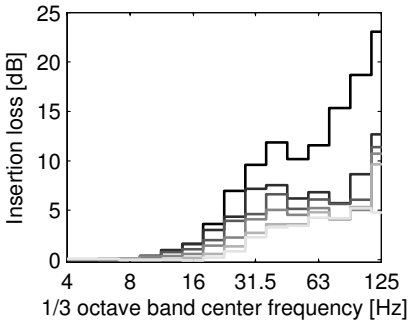

Figure 12: Vertical insertion loss $\widehat{\mathrm{IL}}_z(\mathbf{x},\omega)$ at $8\,\mathrm{m}$, $16\,\mathrm{m}$, $24\,\mathrm{m}$, $32\,\mathrm{m}$, $48\,\mathrm{m}$ and $64\,\mathrm{m}$ from the center of the track (black to light grey lines) due to the passage of a Renfe S599 train at a speed of $160\,\mathrm{km/h}$.

The results in figure 12 can be understood by considering figure 13, which shows a top view of the track, the block of stiffened soil next to the track and the free field. The fixed positions of the dynamic axle loads $\hat{\mathbf{g}}_k(\omega)$ are indicated, as well as two receiver locations $\mathbf{x}_1 = \{x_1, 0, 0\}^{\mathrm{T}}$ and $\mathbf{x}_2 = \{x_2, 0, 0\}^{\mathrm{T}}$ in the free field, with $x_1 < x_2$. At each axle load position, thin grey lines indicate the critical angle $\theta_c(\omega)$, delimiting the area in which the free field vibrations resulting from excitation at the considered position are significantly reduced. Figure 13a illustrates that, at a particular radial frequency $\omega_1 > \omega_c$, the contribution of all axle loads to the free field vibration at the location $\mathbf{x}_1$ is significantly reduced, except for the axle loads $\hat{\mathbf{g}}_{i-1}(\omega)$ to $\hat{\mathbf{g}}_{i+1}(\omega)$ (as $\mathbf{x}_1$ is not situated within the area where a significant reduction can be expected for these axle loads). At the location $\mathbf{x}_2$ further away from the track, however, the transfer of a smaller number of axle loads is effectively mitigated by the block of stiffened soil, as the contribution of the axle loads $\hat{\mathbf{g}}_{i-3}(\omega)$ to $\hat{\mathbf{g}}_{i+3}(\omega)$ will not be reduced. This indicates that subgrade stiffening next to the track is less efficient at locations further away from the track. At a higher radial frequency ω_2 ($\omega_c < \omega_1 < \omega_2$), the critical angle $\theta_c(\omega_2)$ decreases corresponding to equation (7), which implies that the area in which the transfer to the free field is reduced, enlarges. As illustrated in figure 13b, the contribution of all axle loads to the free field vibrations at $\mathbf{x}_1$ will be reduced at this frequency except for $\hat{\mathbf{g}}_i(\omega)$, while the contribution of all axle loads, except $\hat{\mathbf{g}}_{i-1}(\omega)$ to $\hat{\mathbf{g}}_{i+1}(\omega)$, will be reduced at $\mathbf{x}_2$.

The previous discussion reveals that the contribution to the free field vibration of a larger number of axle loads is significantly reduced if a receiver location closer to the track is considered, and for increasing frequencies. These trends are confirmed in figure 12. The free field vibration in the near field is dominated by the closest axle loads (whose contribution will not be reduced), while all axle loads contribute almost equally to the response in the far field. The actual value of the insertion loss $\widehat{\mathrm{IL}}_z(\mathbf{x},\omega)$ obtained at a particular receiver location $\mathbf{x}$ is therefore determined by a trade–off between the relative importance of each axle load and the possibility to mitigate the transfer from the axle load to the free field.

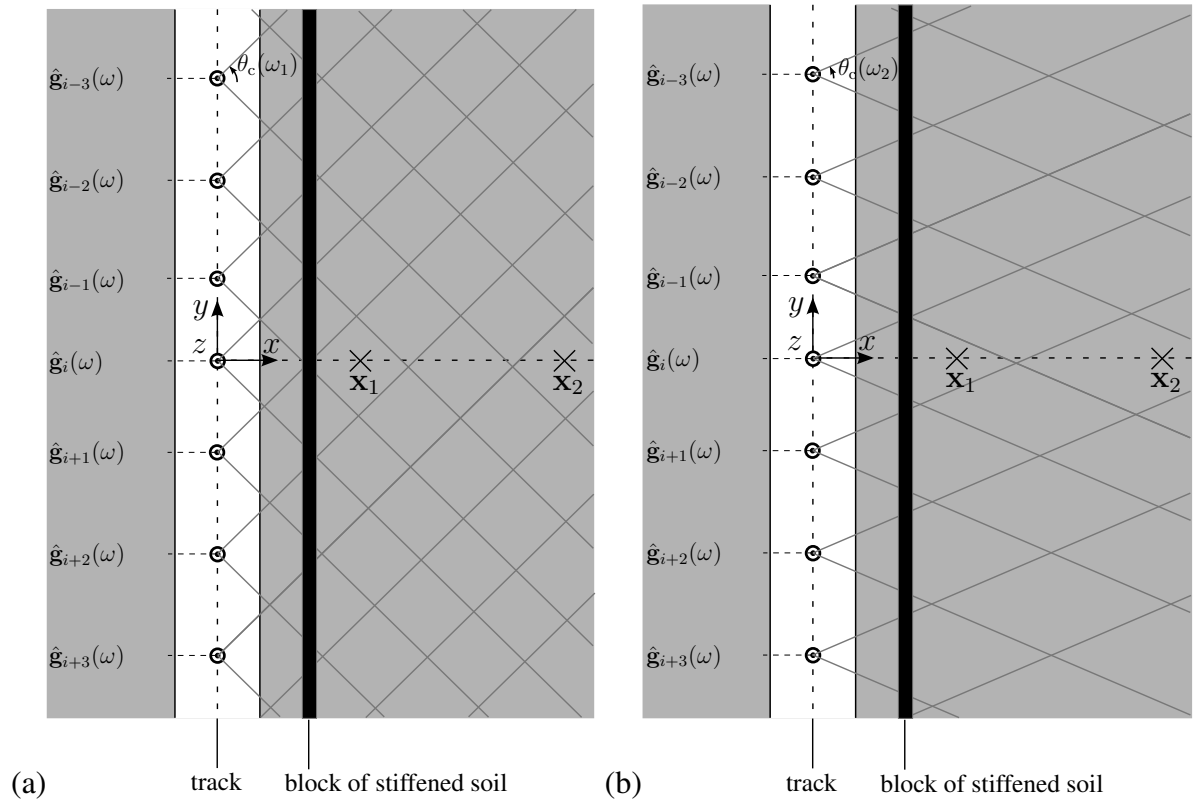

Figure 13: Top view of the track (white), the block of stiffened soil next to the track (black) and the free field (grey). The fixed positions of the dynamic axle loads $\hat{\mathbf{g}}_{i-3}(\omega)$ to $\hat{\mathbf{g}}_{i+3}(\omega)$ are indicated with circles. Superimposed at each axle load position are thin grey lines indicating the critical angle $\theta_{\mathrm{c}}(\omega)$ at a radial frequency (a) ω_1 and (b) ω_2, with $\omega_{\mathrm{c}} < \omega_1 < \omega_2$.

2.7 Influence of the soil stratification

For a layered halfspace, the propagation of Rayleigh waves is dispersive due to the variation of the soil properties with depth, and multiple modes with associated cut-on frequencies exist. The physical mechanism outlined above is still identified in the case of a layered halfspace [33], however, and the region in the $(\overline{k}_y, \omega)$–domain where a significant insertion loss is obtained is bounded by the fundamental Rayleigh wave dispersion curve and the free bending wave dispersion curve. Equations (5) and (7) for the critical frequency and angle, respectively, are still valid, demonstrating their usefulness as a design tool even in the case of a layered halfspace, although C_{R} has to be replaced by $C_{\mathrm{R}}(\omega)$ due to the dispersive nature of the Rayleigh wave. A detailed investigation of case studies involving a layered halfspace can be found in [33].

2.8 Comparison with results from literature

It is instructive to compare the results outlined in this section with previous studies [12, 13, 15, 34, 35]. The current results confirm that subgrade stiffening is more efficient at sites with a soft soil and that increasing the stiffness of the block of soil next to the track is beneficial. It has also been observed in [13] that trenches backfilled with concrete serve as ‘concave lenses’, where a reduction of the vibration levels is predominantly achieved behind and in front of the source. This can be related to the existence of a critical angle, as outlined in subsection 2.4. A more comprehensive explanation of the underlying physics is, however, formulated in the present paper. This study furthermore demonstrates the necessity of 2.5D/3D models to

correctly reveal the underlying physical mechanism and indicates that the use of 2D models is not sufficient.

The proposed mitigation measure can also be compared to alternative methods such as vibration isolation screens. Open trenches aim at reflecting the impinging waves and are effective for trench depths of about one Rayleigh wavelength [10]. The construction of open trenches is, however, for stability reasons limited to shallow depths; the use of in–fill materials allows to increase the depth. If a soft in–fill material is used, the behaviour of a filled trench resembles that of an open trench. The use of a stiff in–fill material, however, results in a wave impeding effect closely related to the physical mechanism outlined in the present paper, and the vibration reduction of such a trench is no longer based on the reflection of incident waves [36].

3 THREE–DIMENSIONAL ANALYSIS

The implementation of subgrade stiffening next to the track is in practice limited to finite dimensions, and the assumption of longitudinal invariance adopted in section 2 is therefore not fulfilled. Accounting for the finite length requires the solution of a fully 3D dynamic soil–structure interaction problem, which is computationally very demanding due to the fact that fully populated unsymmetric matrices arise from classical BE formulations. In order to circumvent the stringent memory and CPU requirements, a fast BE method based on hierarchical matrices ($\mathscr{H}$–matrices) [20] is therefore employed in this section.

3.1 The numerical model

The use of $\mathscr{H}$–matrices provides an elegant way to treat the fully populated matrices arising from the BE method with almost linear complexity [37], as they approximate the original matrices (with an arbitrary prescribed accuracy) by means of data–sparse, memory–efficient representations. The construction of $\mathscr{H}$–matrices is based on the identification of admissible and inadmissible hierarchical cluster pairs in the BE mesh; the partially pivoted adaptive cross approximation (ACA) algorithm [38, 39] is employed to compute low rank approximations of matrix blocks corresponding to admissible cluster pairs. A major advantage of ACA is its purely algebraic character, avoiding the need for (semi–)analytical expressions of the Green's functions employed in the BE formulation (e.g. allowing for the incorporation of Green's functions for a horizontally layered halfspace [20]). The reader is referred to the literature [37, 40, 41] for a detailed description of the methodology regarding $\mathscr{H}$–matrices.

The conventional FE–BE coupling strategy outlined in subsection 2.2 is not well suited to provide an efficient solution of the dynamic soil–structure interaction problem in case $\mathscr{H}$-BE models are employed [42]. An alternative iterative procedure is therefore applied, in which the governing equations of each subdomain are solved separately, while the boundary conditions at the soil–structure interface are updated until convergence is achieved. As demonstrated in [42], a sequential Neumann–Dirichlet algorithm is preferred due to the strong stiffness contrast between the FE and $\mathscr{H}$-BE subdomain (with Neumann boundary conditions imposed on the most stiff subdomain, i.e. the block of stiffened soil).

3.2 The free field impulse response in the frequency–spatial domain

A block of stiffened soil with dimensions $2\,\mathrm{m} \times L_y \times 2\,\mathrm{m}$ and aligned along $x = 5\,\mathrm{m}$ (figure 2) is considered in this subsection. The same dynamic characteristics for the halfspace and the block of stiffened soil as defined in subsection 2.1 are employed. A track is not included in the model, however, as it is inconvenient to combine a 2.5D model for the track with a 3D

model for the block of stiffened soil. This limits the investigation to transfer functions between a unit vertical harmonic point load applied at the origin of the coordinate system and the free field response.

Eight–node solid finite elements are employed for the discretization of the block of stiffened soil, which are coupled to a conforming mesh of four–node quadrilateral boundary elements for the surrounding soil domain. Halfspace Green's functions are employed in the $\mathscr{H}$-BE formulation [20]. The numerical analysis is performed for a block of stiffened soil with a longitudinal length L_y of $15\,\mathrm{m}$, $30\,\mathrm{m}$, and $60\,\mathrm{m}$; the properties of the resulting FE and BE discretizations are listed in table 2.

L_y [m]	# FE elements [−]	# FE nodes [−]	# FE DOFs [−]	# BE elements [−]	# BE nodes [−]	# BE DOFs [−]
15	3840	4941	14823	1568	1637	4911
30	7680	9801	29403	3008	3137	9411
60	15360	19521	58563	5888	6137	18411

Table 2: Properties of the FE and BE discretizations of a block of stiffened soil with a length of $15\,\mathrm{m}$, $30\,\mathrm{m}$, and $60\,\mathrm{m}$.

Figures 14a and 14b–d show the real part of the vertical displacement $\hat{u}_z(\mathbf{x},\omega)$ at a frequency of $15\,\mathrm{Hz}$ in the reference case and in case a block of stiffened soil is included over a finite length L_y, respectively, while the result of a 2.5D calculation based on the assumption of longitudinal invariance is shown in figure 14e. The corresponding vertical insertion loss $\widehat{\mathrm{IL}}_z(\mathbf{x},\omega)$ is also included. The real part of the vertical displacement $\hat{u}_z(\mathbf{x},\omega)$ and the insertion loss $\widehat{\mathrm{IL}}_z(\mathbf{x},\omega)$ at $30\,\mathrm{Hz}$ and $60\,\mathrm{Hz}$ are shown in figures 15 and 16, respectively. The wave impeding effect and the existence of a critical angle can clearly be observed in the invariant cases (figures 14–16e); the area where vibration levels are significantly reduced is enlarged at higher frequencies. It is also evident, however, that stiffening of the soil considering a finite length of $15\,\mathrm{m}$ does not suffice to mimic the dynamic behaviour of an infinitely long block of stiffened soil at $15\,\mathrm{Hz}$ and $30\,\mathrm{Hz}$; a much better correspondence is obtained at $60\,\mathrm{Hz}$. The wavefield in the soil and the insertion loss in the cases where subgrade stiffening is applied over a length of $30\,\mathrm{m}$ or $60\,\mathrm{m}$ agree reasonably well with the result of a 2.5D calculation, at all frequencies under concern.

The observations in figures 14–16 can be interpreted by comparing the length L_y of the block to the free bending wavelength $\lambda_\mathrm{b}(\omega)$ of an infinitely long beam. The latter yields $\lambda_\mathrm{b}(\omega) = 2\pi\left(\frac{Eh^2}{12\rho\omega^2}\right)^{1/4}$ for an Euler–Bernoulli beam, where h is the depth of the block of stiffened soil, and is equal to $14.50\,\mathrm{m}$, $10.25\,\mathrm{m}$, and $7.25\,\mathrm{m}$ at $15\,\mathrm{Hz}$, $30\,\mathrm{Hz}$, and $60\,\mathrm{Hz}$, respectively. This indicates that the length L_y should be approximately two times the free bending wavelength $\lambda_\mathrm{b}(\omega)$ in order to ensure that a finite block can act as a wave impeding barrier and to achieve a vibration reduction efficiency comparable to the invariant case. Even then, however, a finite block is unable to impede the direct transmission of waves from the point of excitation to the free field due to its limited length; this is clearly apparent for a block with a length of $15\,\mathrm{m}$ (figures 14–16b). Furthermore, diffraction occurs at the extremities of the block, and the modal behaviour also affects the wavefield in the soil.

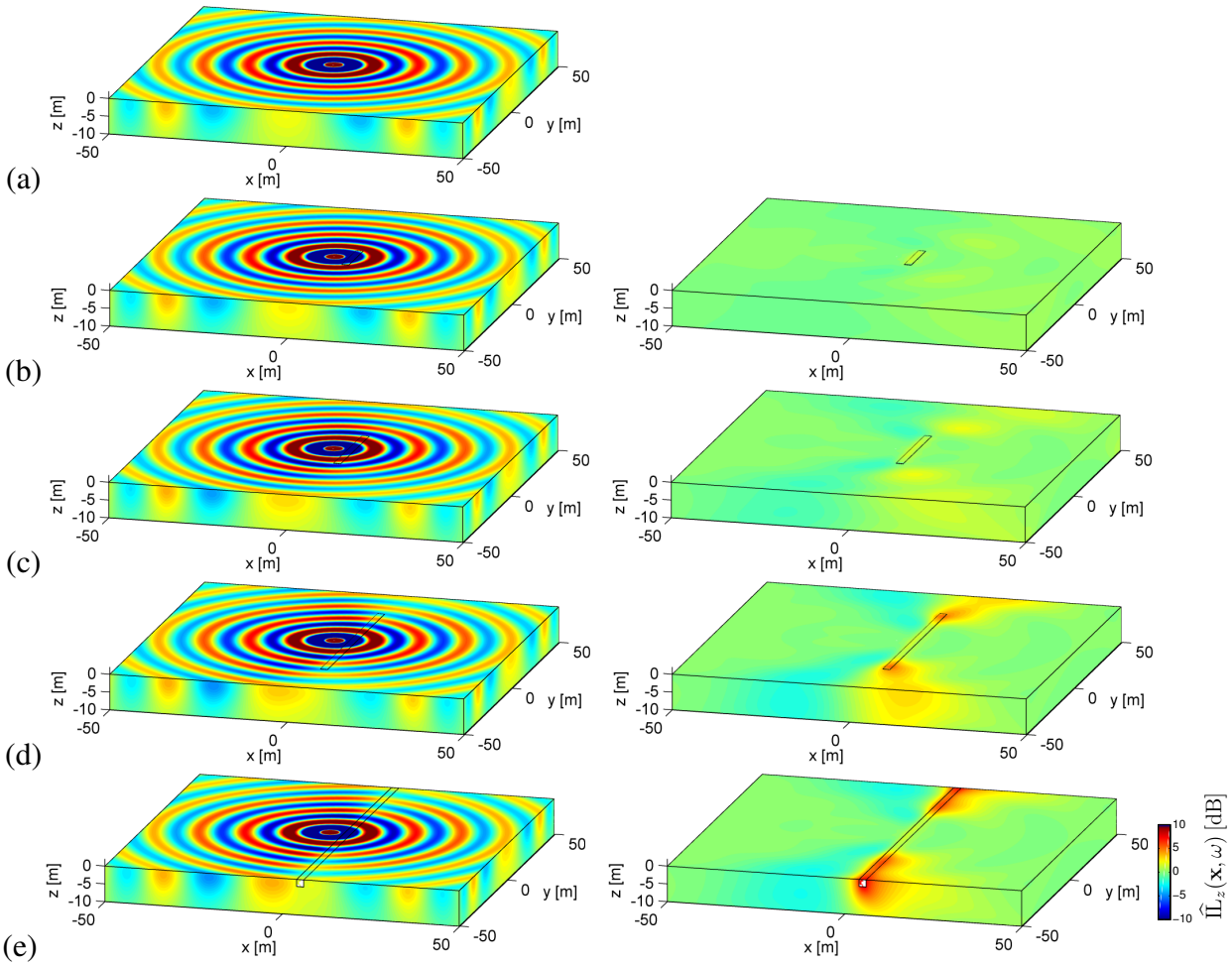

Figure 14: Real part of the vertical displacement $\hat{u}_z(\mathbf{x},\omega)$ due to harmonic excitation at 15 Hz (a) in the reference case and in case a block of stiffened soil is included with a length (b) $L_y = 15\,\mathrm{m}$, (c) $L_y = 30\,\mathrm{m}$, (d) $L_y = 60\,\mathrm{m}$, and (e) $L_y = \infty$ (left hand side). The corresponding insertion loss $\widehat{\mathrm{IL}}_z(\mathbf{x},\omega)$ is shown at the right hand side.

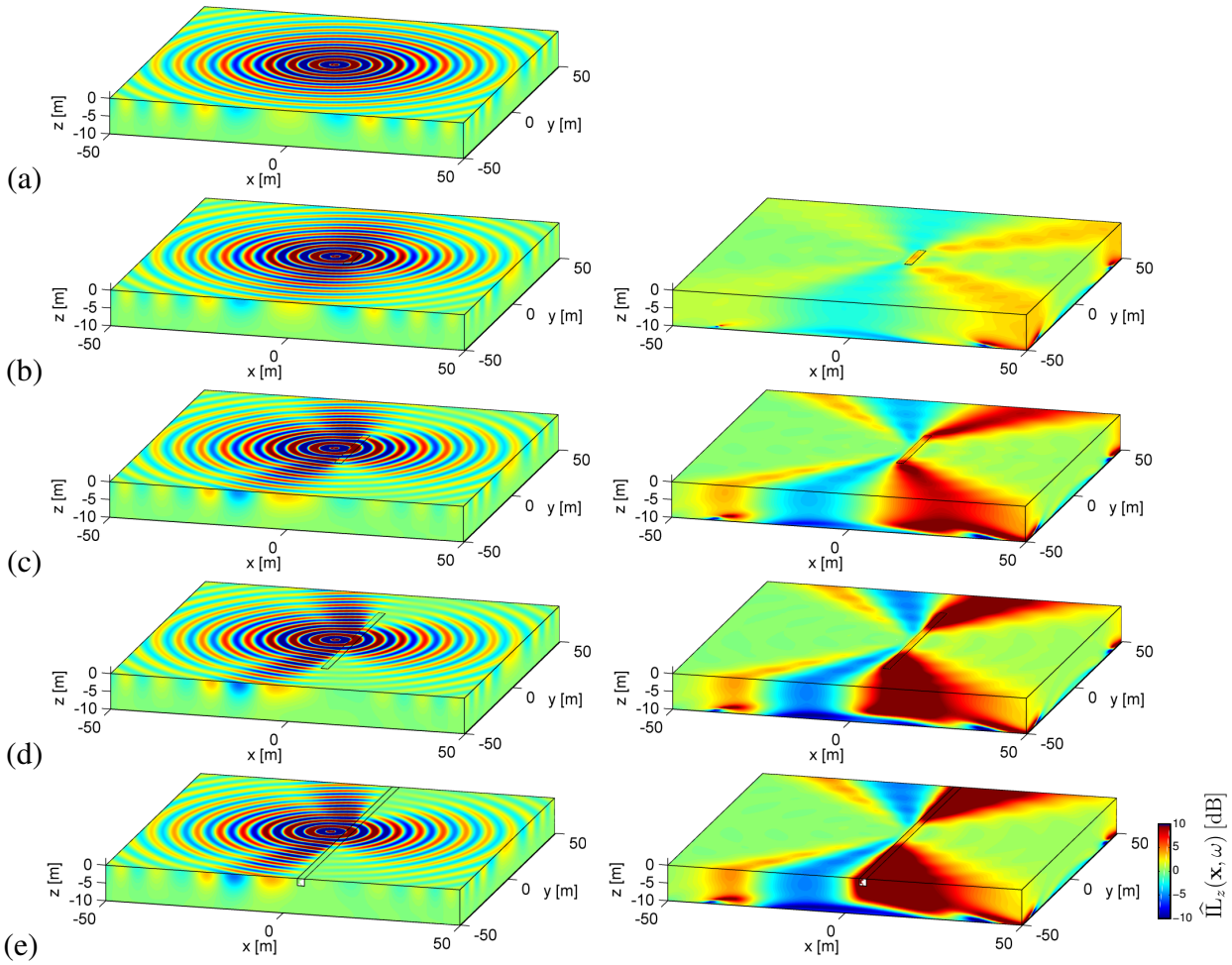

Figure 15: Real part of the vertical displacement $\hat{u}_z(\mathbf{x},\omega)$ due to harmonic excitation at 30 Hz (a) in the reference case and in case a block of stiffened soil is included with a length (b) $L_y = 15\,\mathrm{m}$, (c) $L_y = 30\,\mathrm{m}$, (d) $L_y = 60\,\mathrm{m}$, and (e) $L_y = \infty$ (left hand side). The corresponding insertion loss $\widehat{\mathrm{IL}}_z(\mathbf{x},\omega)$ is shown at the right hand side.

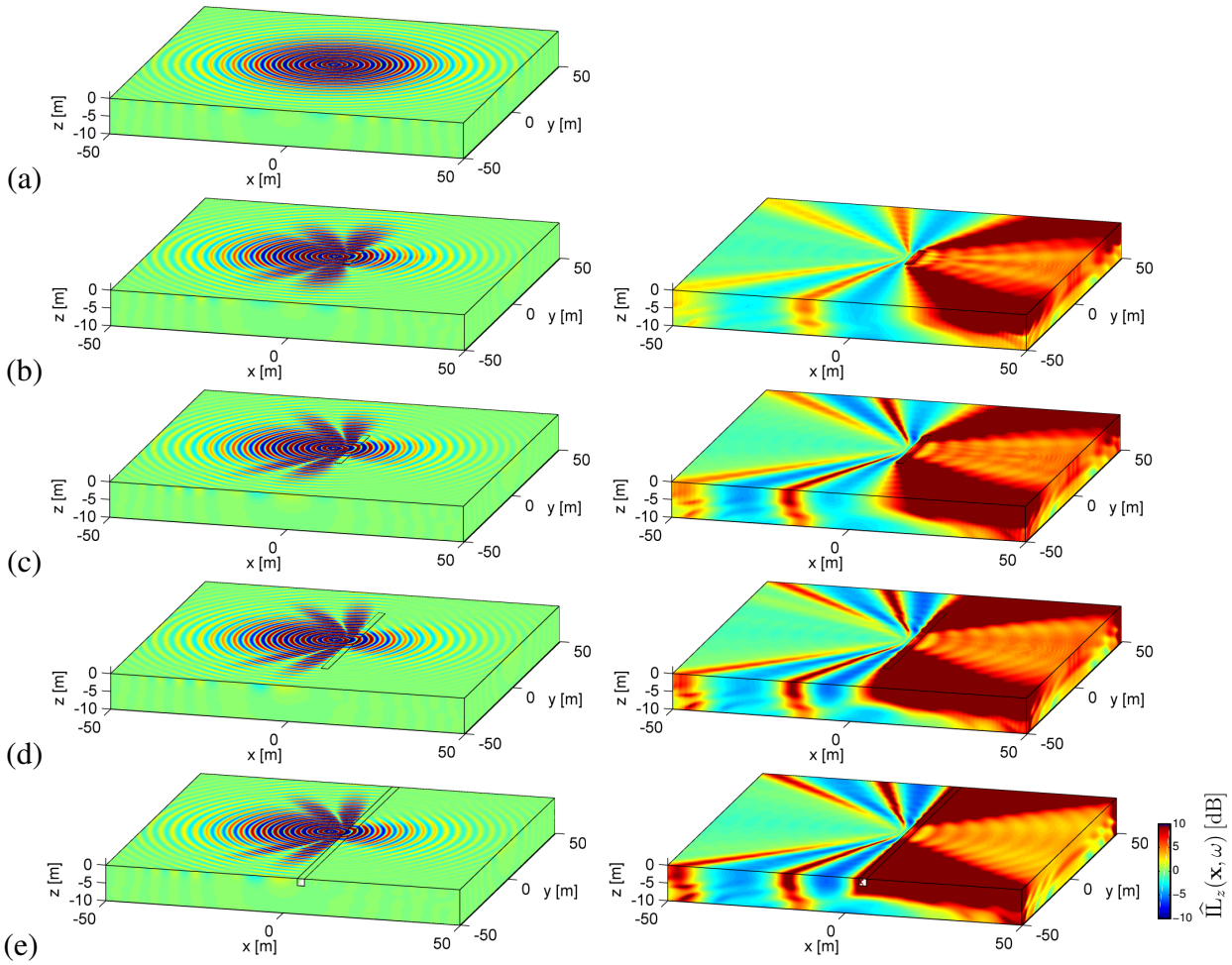

Figure 16: Real part of the vertical displacement $\hat{u}_z(\mathbf{x},\omega)$ due to harmonic excitation at 60 Hz (a) in the reference case and in case a block of stiffened soil is included with a length (b) $L_y = 15\,\mathrm{m}$, (c) $L_y = 30\,\mathrm{m}$, (d) $L_y = 60\,\mathrm{m}$, and (e) $L_y = \infty$ (left hand side). The corresponding insertion loss $\widehat{\mathrm{IL}}_z(\mathbf{x},\omega)$ is shown at the right hand side.

4 CONCLUSIONS

In this paper, the efficiency of subgrade stiffening as a mitigation measure for railway induced vibrations has been investigated. Under the assumption of longitudinal invariance of the geometry, a 2.5D analysis in the frequency–wavenumber domain has clearly illustrated that an infinitely long block of stiffened soil next to the track can act as a wave impeding barrier. The wave impeding effect does, however, critically depend on the relation between the Rayleigh wavelength in the soil and the free bending wavelength in the block of stiffened soil next to the track. This leads to the existence of a critical radial frequency ω_{c} from which this mitigation measure starts to be effective, as well as a critical angle $\theta_{\mathrm{c}}(\omega)$ delimiting the area where the vibration levels are reduced. The expressions for ω_{c} and $\theta_{\mathrm{c}}(\omega)$ have a practical implication, as they allow to assess the expected efficiency of soil stiffening in an early design stage, avoiding an extensive FE–BE calculation. The passage of a train has been investigated as well, revealing that the free field vibration levels can significantly be reduced. It was shown that the number of axle loads of which the contribution to the free field vibration at a certain location is reduced, decreases with the distance from the track and increases with the frequency.

The vibration reduction efficiency in case subgrade stiffening is only implemented along a finite length has finally been assessed through 3D calculations, using a fast BE method based on $\mathscr{H}$–matrices. These calculations indicate that the length of the block should be approximately two times the free bending wavelength of an infinitely long beam in order to ensure that a finite block can act as a wave impeding barrier.

ACKNOWLEDGEMENTS

The results presented in this paper have been obtained within the frame of the EU FP7 project RIVAS (Railway Induced Vibration Abatement Solutions) [9]. The first author is a doctoral fellow and the second author is a postdoctoral fellow of the Research Foundation Flanders (FWO). The financial support is gratefully acknowledged.

REFERENCES

[1] C.J.C. Jones. Use of numerical-models to determine the effectiveness of anti-vibration systems for railways. *Proceedings of the Institution of Civil Engineers-Transport*, 105(1):43–51, 1994.

[2] A.M. Kaynia, C. Madshus, and P. Zackrisson. Ground vibration from high speed trains: prediction and countermeasure. *Journal of Geotechnical and Geoenvironmental Engineering, Proceedings of the ASCE*, 126(6):531–537, 2000.

[3] R. Müller. Mitigation measures for open lines against vibration and ground-borne noise: a Swiss overview. In Burkhard Schulte-Werning, David Thompson, Pierre-Etienne Gautier, Carl Hanson, Brian Hemsworth, James Nelson, Tatsuo Maeda, and Paul de Vos, editors, *Noise and Vibration Mitigation for Rail Transportation Systems*, volume 99 of *Notes on Numerical Fluid Mechanics and Multidisciplinary Design*, pages 264–270. Springer Berlin / Heidelberg, 2008.

[4] R. Hildebrand. Effect of soil stabilization on audible band railway ground vibration. *Soil Dynamics and Earthquake Engineering*, 24:411–424, 2004.

[5] H. Loy. Mitigating vibration using under-sleeper pads. *Railway Gazette International*, 168(4):40–43, 2012.

[6] G. Lombaert, G. Degrande, B. Vanhauwere, B. Vandeborght, and S. François. The control of ground borne vibrations from railway traffic by means of continuous floating slabs. *Journal of Sound and Vibration*, 297(3-5):946–961, 2006.

[7] A. Karlström and A. Boström. Efficiency of trenches along railways for trains moving at sub- or supersonic speeds. *Soil Dynamics and Earthquake Engineering*, 27:625–641, 2007.

[8] J.P. Talbot and H.E.M. Hunt. A generic model for evaluating the performance of base-isolated buildings. *Journal of Low Frequency Noise, Vibration and Active Control*, 22(3):149–160, 2003.

[9] http://www.rivas-project.eu, 2011.

[10] R.D. Woods. Screening of surface waves in soils. *Journal of the Soil Mechanics and Foundation Division, Proceedings of the ASCE*, 94(SM4):951–979, 1968.

[11] K.R. Massarsch. Vibration isolation using gas-filled cushions. In *Proceedings of the Geo-Frontiers 2005 Congress*, Austin, Texas, January 2005. American Society of Civil Engineers.

[12] C.J.C. Jones, D.J. Thompson, and J.I. Andreu-Medina. Initial theoretical study of reducing surface-propagating vibration from trains using earthworks close to the track. In *Proceedings of the 8th International Conference on Structural Dynamics, EURODYN 2011*, pages 684–691, Leuven, Belgium, July 2011.

[13] L. Andersen and S.R.K. Nielsen. Reduction of ground vibration by means of barriers or soil improvement along a railway track. *Soil Dynamics and Earthquake Engineering*, 25:701–716, 2005.

[14] A.T. Peplow and A.M. Kaynia. Prediction and validation of traffic vibration reduction due to cement column stabilization. *Soil Dynamics and Earthquake Engineering*, 27:793–802, 2007.

[15] H.H. Hung, Y.B. Yang, and D.W. Chang. Wave barriers for reduction of train-induced vibrations in soils. *Journal of Geotechnical Engineering, Proceedings of the ASCE*, 130(12):1283–1291, 2004.

[16] X. Sheng, C.J.C. Jones, and D.J. Thompson. Prediction of ground vibration from trains using the wavenumber finite and boundary element methods. *Journal of Sound and Vibration*, 293:575–586, 2006.

[17] V.V. Krylov. Scattering of Rayleigh waves by heavy masses as method of protection against traffic-induced ground vibrations. In H. Takemiya, editor, *Environmental vibrations. Prediction, Monitoring, Mitigation and Evaluation*, pages 393–398. Taylor and Francis Group, London, 2005.

[18] D. Adam, A. Vogel, and A. Zimmermann. Ground improvement techniques beneath existing rail tracks. *Ground Improvement*, 11(4):229–235, 2007.

[19] B.O. Skipp, editor. *Ground dynamics and man made processes*. Thomas Telford, 1998.

[20] P. Coulier, S. François, G. Lombaert, and G. Degrande. A hierarchical boundary element method for elastodynamics based on Green's functions for a horizontally layered halfspace. *Engineering Analysis with Boundary Elements*. Submitted for publication.

[21] J.W.S. Rayleigh. On waves propagated along the plane surface of an elastic solid. *Proceedings of the London Mathematical Society*, 17:4–11, 1887.

[22] G. Lombaert, G. Degrande, J. Kogut, and S. François. The experimental validation of a numerical model for the prediction of railway induced vibrations. *Journal of Sound and Vibration*, 297(3-5):512–535, 2006.

[23] X. Sheng, C.J.C. Jones, and D.J. Thompson. A theoretical model for ground vibration from trains generated by vertical track irregularities. *Journal of Sound and Vibration*, 272(3-5):937–965, 2004.

[24] S. François, M. Schevenels, G. Lombaert, P. Galvín, and G. Degrande. A 2.5D coupled FE-BE methodology for the dynamic interaction between longitudinally invariant structures and a layered halfspace. *Computer Methods in Applied Mechanics and Engineering*, 199(23-24):1536–1548, 2010.

[25] E. Kausel and J.M. Roësset. Stiffness matrices for layered soils. *Bulletin of the Seismological Society of America*, 71(6):1743–1761, 1981.

[26] M. Schevenels, S. François, and G. Degrande. EDT: An ElastoDynamics Toolbox for MATLAB. *Computers & Geosciences*, 35(8):1752–1754, 2009.

[27] P. Hagedorn and A. DasGupta. *Vibrations and Waves in Continuous Mechanical Systems*. John Wiley & Sons, Chichester, United Kingdom, 2007.

[28] L. Cremer, M. Heckl, and B.A.T. Petersson. *Structure-borne sound: Structural vibrations and sound radiation at audio frequencies*. Springer, Berlin, 3rd edition, 2005.

[29] K. Knothe and S.L. Grassie. Modelling of railway track and vehicle/track interaction at high frequencies. *Vehicle Systems Dynamics*, 22: 209–262, 1993.

[30] V.K. Garg and R.V. Dukkipati. *Dynamics of railway vehicle systems*. Academic Press, Canada, 1984.

[31] H. Verbraken, G. Lombaert, and G. Degrande. Verification of an empirical prediction method for railway induced vibrations by means of numerical simulations. *Journal of Sound and Vibration*, 330(8):1692–1703, 2011.

[32] International Organization for Standardization. *ISO 2631-2:1989: Evaluation of human body exposure to whole-body vibration - Part 2: Continuous and shock-induced vibration in buildings (1 to 80 Hz)*, 1989.

[33] P. Coulier, S. François, G. Degrande, and G. Lombaert. Subgrade stiffening next to the track as a wave impeding barrier for railway induced vibrations. *Soil Dynamics and Earthquake Engineering*, 48:119–131, 2013.

[34] S. Ahmad and T.M. Al-Hussaini. Simplified design for vibration screening by open and in-filled trenches. *Journal of Geotechnical Engineering, Proceedings of the ASCE*, 117(1): 67–88, 1991.

[35] R.K. Shrivastava and N.S.V. Kameswara Rao. Response of soil media due to impulse loads and isolation using trenches. *Soil Dynamics and Earthquake Engineering*, 22(6): 695–702, 2002.

[36] S. François, M. Schevenels, B. Thyssen, J. Borgions, and G. Degrande. Design and efficiency of a vibration isolating screen in the soil. *Soil Dynamics and Earthquake Engineering*, 39:113–127, 2012.

[37] L. Grasedyck and W. Hackbusch. Construction and arithmetics of $\mathscr{H}$-matrices. *Computing*, 70:295–334, 2003.

[38] S. Rjasanow and O. Steinbach. *The Fast Solution of Boundary Integral Equations (Mathematical and Analytical Techniques with Applications to Engineering)*. Springer-Verlag New York, 2007.

[39] M. Bebendorf and S. Rjasanow. Adaptive low–rank approximation of collocation matrices. *Computing*, 70:1–24, 2003.

[40] W. Hackbusch. A sparse matrix arithmetic based on $\mathscr{H}$-matrices. Part I: Introduction to $\mathscr{H}$-matrices. *Computing*, 62(2):89–108, 1999.

[41] M. Bebendorf. *Hierarchical Matrices: A Means to Efficiently Solve Elliptic Boundary Value Problems*. Springer Publishing Company, 1st edition, 2008.

[42] P. Coulier, S. François, G. Lombaert, and G. Degrande. A coupled finite element – hierarchical boundary element method based on Green's functions for a horizontally layered halfspace. In N. Heuer and C. Jerez-Hanckes, editors, *Proceedings of the Symposium of the International Association for Boundary Element Methods IABEM 2013*, pages 23–30, Santiago, Chile, January 2013. CD-ROM.